Study of Unsteady, Sphere-Driven, Shock-Induced Combustion for Application to Hypervelocity Airbreathing Propulsion

Erik Axdahl[1], Ajay Kumar[2]
NASA Langley Research Center, Hampton, VA, 23681

and

Alan Wilhite[3]
National Institute of Aerospace, Hampton, VA, 23666

Abstract

A premixed, shock-induced combustion engine has been proposed in the past as a viable option for operating in the Mach 10 to 15 range in a single stage to orbit vehicle. In this approach, a shock is used to initiate combustion in a premixed fuel/air mixture. Apparent advantages over a conventional scramjet engine include a shorter combustor that, in turn, results in reduced weight and heating loads. There are a number of technical challenges that must be understood and resolved for a practical system: premixing of fuel and air upstream of the combustor without premature combustion, understanding and control of instabilities of the shock-induced combustion front, ability to produce sufficient thrust, and the ability to operate over a range of Mach numbers. This study evaluated the stability of the shock-induced combustion front in a model problem of a sphere traveling in a fuel/air mixture at high Mach numbers. A new, rapid analysis method was developed and applied to study such flows. In this method the axisymmetric, body-centric Navier-Stokes equations were expanded about the stagnation streamline of a sphere using the local similarity hypothesis in order to reduce the axisymmetric equations to a quasi-1D set of equations. These reduced sets of equations were solved in the stagnation region for a number of flow conditions in a premixed, hydrogen/air mixture. Predictions from the quasi-1D analysis showed very similar stable or unstable behavior of the shock-induced combustion front as compared to experimental studies and higher-fidelity computational results. This rapid analysis tool could be used in parametric studies to investigate effects of fuel rich/lean mixtures, non-uniformity in mixing, contaminants in the mixture, and different chemistry models.

Nomenclature

a	=	Local speed of sound
A	=	Forward reaction rate coefficient
b	=	Temperature exponent for forward reaction rate
D	=	Damping term
E	=	Total energy
E_a	=	Activation energy
H	=	Total enthalpy
h	=	Sensible enthalpy
$\boldsymbol{M}, \boldsymbol{N}$	=	Flux vectors
$\boldsymbol{Q}$	=	Source vector
R	=	Sphere radius
Re_∞	=	Reynolds number based on freestream quantities
$\boldsymbol{U}$	=	State vector
f	=	Mass fraction

[1] Aerospace Engineer, Hypersonic Airbreathing Propulsion Branch, MS168, Member AIAA
[2] Director, Systems Analysis and Concepts Directorate, MS449, Fellow AIAA
[3] Professor, Department of Aerospace Engineering, Georgia Institute of Technology, Associate Fellow AIAA

k = Local body curvature
M = Mach number
n, s = Normal and tangential coordinates
p = Pressure
q = Heat flux
r = Local cylindrical radius
R_u = Universal gas constant
t = Time
T = Temperature
v, u = Normal and tangential velocity components

α = Body angle measured from stagnation streamline
β = Non-dimensional height measured from stagnation streamline
γ = Ratio of specific heats
λ = Non-dimensional distance measured from sphere center
μ = Dynamic viscosity
$\dot{\omega}_i$ = Production rate of species i
Π_{ij} = Stress tensor
ρ = Density

I. Introduction

Access to higher Mach numbers is one of the goals that drive current research in supersonic combustion ramjets (i.e scramjets). The benefit of operating at higher Mach numbers is evident when considering the example of a scramjet that is integrated in a single stage to orbit space-access vehicle[1]. For example, at Mach 10 such a vehicle has attained approximately 15% of the required kinetic energy to reach low Earth orbit (LEO) before transition to rocket-mode while at Mach 15 it has reached 30%. To date, most research and design concepts are projected to operate up to Mach 10 before experiencing a significant reduction in or loss of performance. This is because increasing the freestream Mach number reduces the time that is allowed for diffusive mixing and combustion. One of the simplest ways to mitigate this problem is by elongating the combustor; however, this increases the mass of the vehicle considerably as the combustor tends to be a significant mass element of the engine.

The utilization of premixed, shock-induced combustion (PMSIC) is one method that shows promise in driving airbreathing propulsion to higher Mach numbers (i.e. hypervelocity propulsion). In a PMSIC engine concept (see Figure 1), the fuel is injected on the forebody of the vehicle rather than in the combustor, as is the case for conventional scramjets. The fuel and air undergo mixing and then travel through a strong, oblique shock wave from the cowl lip that causes auto-ignition and subsequent combustion of the fuel-air mixture. Apparent advantages of the PMSIC engine concept are a shorter combustor length that, in turn, results in reduced weight and heating loads. Assuming the vehicle is boosted to hypervelocity speeds, the isolator component typically found in scramjet concepts is able to be removed, further amplifying these benefits. Other benefits include improved pressure recovery at the combustor when hydrogen fuel is used[2]. These benefits translate into access to much higher Mach numbers than conventional scramjets and, therefore, delayed staging when used for space access.

When considering the problem of injecting fuel in the inlet, there are multiple technical challenges that must be overcome to arrive at a practical concept. These challenges include

- **Inlet auto-ignition** – Because the fuel is injected on the forebody of the vehicle, it is possible for the fuel/air mixture to experience pre-ignition in the hot boundary layer on the surface. Large amounts of drag and heating are then experienced on the forebody, resulting in significant performance losses in the engine.
- **Mixing losses** – The premixed fuel-air stream may not be uniformly mixed or may be lost due to inlet spillage. These non-uniformities may have an important effect on the stability of the ignition and combustion.
- **Shock wave stability** – Depending on the flow conditions, a weak or strong coupling between the reaction front and the shock wave inducing combustion may occur, resulting in instabilities of the reaction front and the shock wave. The presence of these instabilities would have consequences ranging from reduced performance to engine unstart.

The focus of this paper is to examine shock wave stability in a representative model problem of hydrogen/air PMSIC ahead of a blunt projectile traveling at near-hypersonic speeds. Previous numerical and experimental work has been conducted on this particular problem with one observation being that instabilities in the flow emanate from the stagnation region of the body and propagate downstream[3]. This study takes advantage of this observation and re-formulates the blunt-body problem in a quasi-1D manner. In this formulation, the flow was numerically simulated only along the stagnation streamline with pertinent gradient values normal to the centerline included as well. This approach drastically reduced computational time over multi-dimensional simulations, thus allowing rapid studies of the effects of different parameters (e.g. free stream pressure, velocity, nose radius, varying stoichiometry, non-uniformity in mixing, contaminants, chemistry models, etc.). This rapid computational capability allows the analyst to quickly parameterize the behavior of the system over a wide range of design variables. This is important for identifying safe regimes where the flame may be stable for conditions found at the combustor during hypervelocity flight. As a result, this formulation should be a valid starting point for higher-fidelity flowpath and trajectory designs. For this study, the behavior of the reaction and shock fronts was evaluated over a wide range of velocities relevant to past experiments. The effect on stability of changing inflow stoichiometry was also studied.

II. Body-Driven, Premixed Shock-Induced Combustion

To date there have been many experimental and numerical studies of the blunt-body PMSIC phenomenon. Early experimental work in the 1960's and 70's[4-7] provided observations of PMSIC in a controlled environment and also classified different regimes of combustion and shock instability. The first regime is a stable regime that exhibits smooth, uncoupled reaction and shock fronts with no unsteady motion. The stable regime will not be discussed further in this section. The next regime is a regular, unsteady regime in which a ``corrugated'' reaction front appears that is periodic and forms a small-amplitude oscillation in the bow shock. Finally, a large-amplitude, unsteady regime is observed that is non-periodic and exhibits significant coupling of the bow shock and reaction front such that the reaction zone pushes the bow shock far upstream before retreating back to its original position. Examples of these regimes may be found in Figures 3, 4, and 5 and will be discussed in greater detail later.

The mechanism of the regular, unsteady regime was initially synthesized from experiments by McVey and Toong[5] and was later refined by the numerical studies of Matsuo and Fujiwara[8] to include the effect of reflected compression waves from the body. In this regime, pressure waves created by the inception of a new reaction front travel both toward the body and the bow shock. Collision of the pressure wave with the bow shock pushes the shock upstream and reflects a contact discontinuity. Upstream of the contact discontinuity is gas with higher temperature (and therefore shorter ignition delay time) which eventually results in the formation of a second reaction zone ahead of the original one and the production of another set of pressure waves. Once the contact discontinuity meets the original reaction front it is extinguished, thereby generating expansion waves. This behavior is repeated periodically in a staggered manner.

A large-amplitude, unsteady mechanism was proposed by Alpert and Toong[7] along with experiments documenting its behavior. This model was later updated through numerical studies of Matsuo, *et al.*[9] It was proposed that the instability exhibited in this regime finds root in the significantly higher heat release caused by the harsher free stream conditions. This heat release at the reaction inception point causes a superdetonation to travel towards the bow shock and a retonation to travel toward the body. In this context, a retonation is a strong pressure wave that travels downstream through the burned gases while a superdetonation occurs where the reaction front and its initiating shock wave are tightly coupled. Interaction of the superdetonation with the bow shock causes a retonation and contact discontinuity to travel toward the wall while the superdetonation heaves the bow shock upstream in a large-amplitude manner. Upon relaxation of the bow shock and the reaction front, a mechanism similar to that of the regular, unsteady regime is observed in the creation of a new reaction front. This cycle repeats non-periodically with an effective period greater than that of the regular regime.

Other numerical studies have shed light on the physical behavior and computation of body-driven PMSIC. Wilson and MacCormack[10] found in simulating the experiments of Lehr[6] that there was significant sensitivity both to grid spacing and to reaction rates in the Jachimowski model[11]. Another study by Wilson and Sussman[12] applied a logarithmic transformation to the species continuity equations to provide enhanced solution accuracy for coarser grids. Investigations by Ahuja, *et al* [13-15] simulated the Lehr experiments at and above the detonation velocity of the mixture (Mach 5.11 and 6.46, respectively). In their studies, the Matsuo regular regime model for the Mach 5.11 case was verified and the frequencies in the simulated flow field, determined using a Fourier transform, compared favorably with experiment. For the overdrive case of Mach 6.46 it was shown that the period of instability was

reduced to such an extent that the flow field appears macroscopically stable and the reaction front had merged with the bow shock. These numerical results were also verified against experimental data.

III. Simulation Methodology

Governing Equations

The axisymmetric Navier-Stokes equations and species conservation equations in the body-oriented coordinate system shown in Figure 2 can be written as

$$\frac{\partial \mathbf{U}}{\partial t}+\frac{\partial \mathbf{M}}{\partial s}+\frac{\partial \mathbf{N}}{\partial n}+\mathbf{Q}=0 \tag{1}$$

The state vector (**U**), flux vectors (**M, N**), and source term vector (**Q**) are expressed in non-dimensional form as

$$\mathbf{U}=\lambda\begin{pmatrix}\rho\\ \rho u\\ \rho v\\ \rho E\\ \rho f_i\end{pmatrix} \tag{2}$$

$$\mathbf{M}=\begin{pmatrix}\rho u\\ \rho u^2-\Pi_{11}\\ \rho uv-\Pi_{12}\\ \rho Eu+q_1-u\Pi_{11}-v\Pi_{21}\\ \rho f_i u\end{pmatrix} \tag{3}$$

$$\mathbf{N}=\lambda\begin{pmatrix}\rho v\\ \rho uv-\Pi_{21}\\ \rho v^2-\Pi_{22}\\ \rho Ev+q_2-u\Pi_{12}-v\Pi_{22}\\ \rho f_i v\end{pmatrix} \tag{4}$$

$$\mathbf{Q}=\frac{1}{\beta}(\lambda\mathbf{M}\cos\alpha+\mathbf{N}\sin\alpha)+\frac{1}{\beta}\begin{pmatrix}0\\ \beta k\rho uv+\lambda\Pi_{33}\cos\alpha-\beta k\Pi_{12}\\ -\beta k\rho u^2+\beta k\Pi_{11}+\lambda\,\Pi_{33}\sin\alpha\\ 0\\ -\beta\lambda\dot{\omega}_i\end{pmatrix} \tag{5}$$

where $\lambda=1+nk$, $\beta=r+n\cos\alpha$. In these equations, variables have been non-dimensionalized with respect to free stream velocity, temperature, density, and body radius.

In order to arrive at the quasi-1D form of equations, a local similarity postulation[16, 17] was used in the stagnation region. Under this approach, flow variables were expanded in a series about the axis of symmetry by

$$\begin{array}{rcl|l}\rho(s,n,t) & = & \rho_1(n,t) & +\rho_2(n,t)\sin^2\alpha+\cdots\\ p(s,n,t) & = & p_1(n,t)+p_2(n,t)\sin^2\alpha & +p_3(n,t)\sin^4\alpha+\cdots\\ H(s,n,t) & = & H_1(n,t) & +H_2(n,t)\sin^2\alpha+\cdots\\ u(s,n,t) & = & u_1(n,t)\sin\alpha & +u_2(n,t)\sin^3\alpha+\cdots\\ v(s,n,t) & = & v_1(n,t)\cos\alpha & +v_2(n,t)\cos\alpha\sin^2\alpha+\cdots\\ & & (\text{First Truncation}) & \end{array} \tag{6}$$

Note that the retention of the second order term in pressure is warranted by the order of magnitude analysis. The expansions given in Equation (6) have had a small-angle approximation applied due to the result that $s=\alpha$ for a non-dimensionalized sphere. The solution variables in the first truncation have a simplified notation where terms in

the expansion equal to zero have been removed and the remaining solution variables and their derivatives have simply been given the names of the expanded state variable with subscripts. Here u_1 is actually the first derivative of velocity with respect to s and p_2 is the second derivative of pressure with respect to s. All other subscripted variables in the first truncation are equal to their respective state variables.

Retaining terms only to the first truncation shown in Equation (6) and substituting into Equations (3) - (5), the following set of equations is obtained for a sphere by equating the coefficients of like powers of α. Note that on the stagnation streamline $\alpha = 0$. The governing equations are reduced to the form

$$\frac{\partial \mathbf{U}'}{\partial t} + \frac{\partial \mathbf{N}'}{\partial n} + \mathbf{Q}' = 0 \tag{7}$$

where now the solution is a function only of time and distance normal to the surface. Note that the primes have been added to indicate the quasi-1D form of the vectors. The state vector has the form

$$\mathbf{U}' = \begin{pmatrix} \rho_1 \\ \rho_1 u_1 \\ \rho_1 v_1 \\ \rho_1 H_1 - p_1 \\ \rho_1 f_i \end{pmatrix} \tag{8}$$

The flux vector is split into contributing terms by

$$\mathbf{N}' = \mathbf{N}'_{\mathbf{i}} + \mathbf{N}'_{\mathbf{v}} + \mathbf{N}'_{\mathbf{c}} \tag{9}$$

where each term represents the inviscid, viscous, and chemical contributions to the flux, respectively. These terms are given by

$$\mathbf{N}'_{\mathbf{i}} = \begin{pmatrix} \rho_1 v_1 \\ \rho_1 u_1 v_1 \\ \rho_1 v_1^2 + p_1 \\ \rho_1 v_1 H_1 \\ 0 \end{pmatrix} \tag{10}$$

$$\mathbf{N}'_{\mathbf{v}} = \begin{pmatrix} 0 \\ -\frac{\mu_1}{Re_\infty}\left(\frac{\partial u_1}{\partial n} - \frac{u_1 + v_1}{1+n}\right) \\ -\frac{4}{3}\frac{\mu_1}{Re_\infty}\left(\frac{\partial v_1}{\partial n} - \frac{u_1 + v_1}{1+n}\right) \\ -\frac{2}{1+n}\frac{\mu_1}{\sigma Re_\infty}\frac{\partial h_1}{\partial n} \\ 0 \end{pmatrix} \tag{11}$$

$$\mathbf{N}'_{\mathbf{c}} = \begin{pmatrix} 0 \\ 0 \\ 0 \\ 0 \\ \rho_1 f_i v_1 \end{pmatrix} \tag{12}$$

In a similar fashion the source term is split up as

$$\mathbf{Q'_i} = \frac{u_1 + v_1}{1+n}\begin{pmatrix} 2\rho_1 \\ 3\rho_1 u_1 + \dfrac{2}{u_1 + v_1}p_2 \\ 2\rho_1 v_1 \\ 2\rho_1 H_1 \\ 0 \end{pmatrix} \tag{13}$$

$$\mathbf{Q'_v} = \begin{pmatrix} 0 \\ \dfrac{\mu_1}{(1+n)Re_\infty}\left(\dfrac{11}{3}\dfrac{u_1 + v_1}{1+n} - \dfrac{2}{3}\dfrac{\partial v_1}{\partial n} - 3\dfrac{\partial u_1}{\partial n}\right) \\ \dfrac{\mu_1}{(1+n)Re_\infty}\left(6\dfrac{u_1 + v_1}{1+n} - 4\dfrac{\partial v_1}{\partial n} - 2\dfrac{\partial u_1}{\partial n}\right) \\ -\dfrac{2}{1+n}\dfrac{\mu_1}{\sigma Re_\infty}\dfrac{\partial h_1}{\partial n} - \dfrac{\mu_1}{Re_\infty}\left[\dfrac{4}{3}(u_1 + v_1)\left(\dfrac{u_1 + v_1}{1+n} - \dfrac{\partial v_1}{\partial n}\right) + 2v_1\left(\dfrac{\partial u_1}{\partial n} - \dfrac{u_1 + v_1}{1+n}\right)\right] \\ 0 \end{pmatrix} \tag{14}$$

$$\mathbf{Q'_c} = \begin{pmatrix} 0 \\ 0 \\ 0 \\ 0 \\ 0 \\ \dfrac{2\rho_1 f_i(u_1 + v_1)}{1+n} - \dot{\omega}_i \end{pmatrix} \tag{15}$$

An additional equation is required for the solution of p_2, given by

$$\frac{\partial p_2}{\partial n} = -\frac{\partial p_1}{\partial n} + \frac{\rho_1 u_1 (u_1 + v_1)}{1+n} \tag{16}$$

which comes from the *s*-momentum equation. This equation is decoupled from the Navier-Stokes equations and can be solved separately in a non-lagging manner.

Numerical approach

The governing equations are integrated over the convective time step using two methods. First, the convective and diffusive terms in the governing equations are solved using MacCormack's predictor-corrector technique[18]. This scheme is second-order accurate in both time and space. As the current implementation employs shock capturing, numerical damping is required to control the resulting dispersive error occurring around areas of large gradient in the solution such as the shock front. The terms describing numerical damping at each grid point have the TVD-like form[19]

$$D_\phi = \frac{S_\phi \left|\phi_{j+1} - 2\phi_j + \phi_{j-1}\right|}{(1 - \omega_\phi)\phi_{TVD} + \omega_\phi \Phi_j}(v_j + a_j)\frac{\partial \mathbf{U'}}{\partial n} \tag{17}$$

where

$$\phi_{TVD} = \left|\phi_{j+1} + \phi_j\right| + \left|\phi_j - \phi_{j-1}\right| \tag{18}$$

$$\Phi_j = \phi_{j+1} + 2\phi_j + \phi_{j-1} \tag{19}$$

$$a_j = \sqrt{\gamma \frac{(p_1)_j}{(\rho_1)_j}} \tag{20}$$

and where S_ϕ and ω_ϕ are damping constants that have values the analyst may choose—for this study they were both set to 0.3 after some manual optimization. The placeholder variable ϕ represents any variable used in the damping

expression, for example pressure, temperature, or species concentration. If multiple variables are used in the damping scheme simply add each to the PDE, which at spatial step *i* takes the form

$$\left(\frac{\partial \mathbf{U}'}{\partial t}\right)_j^t + \left[\frac{\partial\left(\mathbf{N}' - D_{\phi_1} - D_{\phi_2} - \cdots\right)}{\partial n}\right]_j^t + \left(\mathbf{Q}'\right)_j^t = 0 \tag{21}$$

The damping term should be updated for each step of the MacCormack method. Note that when differencing the state vector in Equation (17), the opposite type of differencing should be used than what is used in the current MacCormack step. For example, if forward differencing is currently being used in the MacCormack step, backwards differencing should be used for the damping term and vice versa.

Once the convective terms have been integrated, changes in species composition at each grid point due to chemistry are then computed. In the current implementation, the chemical reactions are integrated over the convective time step using a quasi-steady-state solution method described by Mott, *et al.*[20] The chemical model used in this study is a reduced form of the hydrogen-air model developed by Jachimowski[11]. It is an 8-species, 13-reaction model which includes the chemical species H, O, OH, H_2O, HO_2, H_2, O_2, and N_2. The species N_2 only acts as a diluent species unless otherwise stated. The species H_2O_2 is excluded from the present mechanism due to its slow rate of formation in high-temperature combustion applications[21]. Table 1 shows the mechanism used in this study and the parameters used in the Arrhenius equation for each reaction.

Table 1. An 8-species, 13-reaction chemical model for H_2-air combustion.[11]

	Reaction	A	b	E_a/1000
1	$O_2 + H_2 \leftrightarrows OH + OH$	1.70E+13	0.0	48.00
2	$OH + H2 \leftrightarrows H + H_2O$	2.20E+13	0.0	5.15
3	$H + O_2 \leftrightarrows OH + O$	2.60E+13	0.0	16.8
4	$O + H_2 \leftrightarrows H + OH$	1.80E+10	1.0	8.90
5	$OH + OH \leftrightarrows H_2O + O$	6.30E+12	0.0	1.09
6	$OH + H + M \leftrightarrows H_2O + M$	2.20E+22	-2.0	0.00
7	$O + H + M \leftrightarrows OH + M$	6.00E+16	-0.6	0.00
8	$H + H + M \leftrightarrows H_2 + M$	6.40E+17	-1.0	0.00
9	$H + O_2 + M \leftrightarrows HO_2 + M$	2.10E+15	0.0	-1.00
10	$HO_2 + H \leftrightarrows H_2 + O_2$	1.30E+13	0.0	0.00
11	$HO_2 + H \leftrightarrows OH + OH$	1.40E+14	0.0	1.08
12	$HO_2 + O \leftrightarrows OH + O_2$	1.50E+13	0.0	0.95
13	$HO_2 + OH \leftrightarrows H_2O + O_2$	8.00E+12	0.0	0.00

Species: H, O, OH, O_2, H_2, H_2O, HO_2, N_2

The listed forward rate coefficients satisfy the Arrhenius form $k_f = AT^b e^{-\frac{E_a}{R_u T}}$ and are in cgs units.
Third body coefficients for each reaction are as follows:
(6) $H_2O = 6$; (7) $H_2O = 5$; (8) $H_2O = 6$, $H_2 = 2$; (9) $H_2O = 16$, $H_2 = 2$

The inflow boundary condition simply takes on freestream values of the variables due to the method being shock capturing. u_1, ρ_1, and T_1 were set to one, v_1 was set to negative one, p_2 was set to zero, and p_1 was obtained from the non-dimensional equation of state. The initial species composition across the domain was that of the freestream. At the wall, v_1 was set to zero due to impermeability, p_1 was set using a zero gradient assumption, and u_1 was set either to be zero (viscous, no slip) or equal the value contained in the nearest grid point (slip). Temperature was either set using an adiabatic assumption or set to be constant when considering cases of a particular wall temperature. Density at the wall was determined using the perfect gas relation at the wall.

The initialization strategy was the same for each case being considered. The values of wall pressure and both velocities were set to change linearly from their freestream value to a guess of their wall value. Total enthalpy was assumed to be constant along the domain at the freestream value, from which initial conditions of temperature, sensible enthalpy, density were then determined. Species composition across the domain was also assumed to be constant at the inflow value across the solution domain.

A 400-point, equally spaced grid was found to be sufficient in this study in order to resolve the fine details of the flow. A CFL number of 0.4 with global time stepping was chosen for the results presented in this paper. All simulations were conducted on a high performance workstation with code written in Fortran. Because of the

unsteady phenomena present in the flow, limit cycling in the residual calculation is typically present with the exception of cases with a stable reaction front. The simulations were considered to be converged when the transient features of the flow were eliminated.

IV. Results and Comparison

Qualitative Experimental and Numerical Comparison

The experiments of Ruegg and Dorsey[4] were simulated using the quasi-1D code in order to qualitatively assess the suitability of the proposed analysis method. Ruegg and Dorsey conducted early experiments on PMSIC by firing spherical, 20 mm diameter projectiles into a stoichiometric hydrogen-air mixture in the vicinity of Mach 5 at pressures ranging from 0.1 to 0.5 atm. Over the range of experimental conditions investigated, three distinct regimes of behavior of the reaction/shock front system were observed: stable; regular, unsteady; and large-disturbance, unsteady. A qualitative comparison between the quasi-1D simulation results and experimental shadowgraphs at the conditions in Table 2 will now be made. The simulated results consist of an evolution of water mass fraction and pressure on the stagnation streamline as a function of non-dimensionalized time and distance (n) from the surface of the projectile.

Table 2. Selected Ruegg and Dorsey experimental conditions for a 20 mm diameter, spherical projectile fired into premixed, stoichiometric hydrogen/air[4].

Case	M_∞	p_∞ (atm)	T_∞ (K)	Stability Regime
1	5	0.10	300	Stable
2	4.9	0.25	300	Regular, Unsteady
3	4.3	0.50	300	Large Disturbance, Unsteady

Figure 3 shows quasi-1D simulation and experimental results for the stable regime of oscillation. The simulated and experimental results indicate reaction and shock front locations that are invariant with time. This invariance is observed experimentally by smooth shock and reaction fronts. The reaction and shock fronts are separated by a relatively large induction distance with no direct interaction between the two beyond the shock wave raising the temperature of the hydrogen/air mixture above its autoignition limit. There is qualitative agreement between simulation and experiment for this case.

The regular instability regime is reproduced in Figure 4. The experimental shadowgraph shows a corrugated pattern in the wake of the sphere caused by an oscillation in density due to the periodic creation of new reaction fronts in the stagnation region of the flow. Between the corrugated, burned region of gas and the shock wave lies a region of unburned gas. This is due to the presence of an observable induction distance between the bow shock and the reaction front. Lines of density variation in the unburned region are due to periodic contact discontinuities traveling from the bow shock to the beginning of each new reaction zone. The contact discontinuities are not visible in the simulated results in this figure because contour lines of pressure are shown (pressure being equal on both sides of a contact discontinuity). The contact discontinuities in the computations will be visible in later figures when the computed results are compared to established 1D mechanisms. There is qualitative agreement between the experiment and the present computations because the physical mechanism observed in the simulated results match the flow features witnessed in the experimental shadowgraph.

The large-disturbance instability regime is shown in Figure 5. Experimental results of the flow at the Case 3 condition show a large-amplitude heaving of both the bow shock and the reaction front. Both the bow shock and reaction zone oscillate with a much lower frequency than that observed in the regular regime and apparently non-periodic features are visible in the shadowgraph. Although both the experiment and the present numerical results show large amplitude behavior, it is difficult to isolate other features to determine how well the quasi-1D simulation is performing. For further comparison, the present results are compared to a higher-fidelity, 2D simulation. Figure 6 shows a zoomed-in view of a section of the present quasi-1D simulation compared to a segment of a simulation at the same conditions conducted by Matsuo and Fujii[22]. These images show contours of density as a function of time and distance along the stagnation streamline. The present results show a striking agreement with the high-fidelity numerical result and clearly show coinciding features of reaction shocks, retonations, contact discontinuities, and a superdetonation as the bow shock is penetrated by the reaction front. These features will be discussed in further detail later, but for now it appears that the quasi-1D results are capable of predicting the large-disturbance instability regime.

Investigation of Reaction Front Oscillation Frequency

The current analysis approach has been applied to simulate the ballistic experiments conducted by H.F. Lehr[6] in which 15 mm diameter projectiles were fired into a stationary, premixed, stoichiometric hydrogen/air mixture at near-hypersonic speeds. The ambient conditions of the fuel-air mixture had a static temperature and pressure of 292 K and 0.42 atm, respectively. Before the results from the current study are discussed, some quick observations are made about Lehr's experiments and the numerical simulations by Sussman[23].

Lehr investigated the behavior of the reacting system over a wide range of velocities, 1685 to 2058 m/s. For each case, the frequency of oscillation of the reaction front was determined using shadowgraph images and considering the distance between successive striations in the wake of the sphere. Lehr found that as projectile velocity increased the frequency of oscillation increased monotonically. At high projectile velocities an overdriven detonation occurred which caused an apparently stable reaction front.

The Chapman-Jouguet detonation velocity of a stoichiometric hydrogen-air mixture with initial conditions as that of the Lehr experiments was calculated to be 1957 m/s using the Chemical Equilibrium with Applications (CEA) program developed at NASA Glenn by McBride and Gordon[24, 25]. This velocity is sensitive to species present—in this case only the species H, O, OH, H_2O, HO_2, H_2, O_2, and N_2 were allowed as product species. The experimental value reported by Lehr was 2030 m/s, corresponding to the velocity past which oscillations in the reaction front were no longer visible. It should be noted, however, that other analyses have established that oscillations might occur above the Chapman-Jouguet detonation velocity. For example, the experiments of Alpert and Toong[7] found oscillations in the overdriven range of flight and modern numerical analyses have also substantiated this observation[13-15, 23].

Sussman[23] simulated the axisymmetric flow around a 15 mm diameter sphere at the same ambient conditions and freestream velocities studied by Lehr using an upwind, TVD scheme. The oncoming flow is composed of a stoichiometric hydrogen-air mixture. In general, the numerical results of Sussman matched well with the experimental results with the exception of cases near the high velocity limit. A large discrepancy was observed at 2058 m/s, which was postulated to be due to the method of interpreting the experimental frequency at that point. However, the experimental oscillation frequency at this point was successfully replicated in numerical work done around the same time by Ahuja[13-15]. At a projectile velocity of 2119 m/s, Lehr showed no oscillation although the numerical work by Ahuja showed oscillations occurring all the way to 2605 m/s; however, at this point they were of very small amplitude and located away from the stagnation streamline. Sussman was able to simulate oscillations for the 2119 m/s case but not for the 2605 m/s case.

Figure 7 shows results from the quasi-1D simulations over the velocity range studied by Lehr and Sussman. Note that due to the reduced computing requirements of the quasi-1D simulation, a large number of cases are computed over the velocity range of the experiment versus previous numerical studies. In doing so, a better idea as to the general shape and limits of the parameter space is obtained. It is observed that, in general, the present results are in reasonable agreement with experimental results and higher-order simulations. Overall the quasi-1D simulations over-predict oscillation frequencies by 17%-34%. In all cases the overall behavior of the flow is predicted (e.g. regime of instability) well.

Table 3. Oscillation frequencies from experiment and numerical investigations.

Projectile Velocity (m/s)	Lehr[6] (kHz)	Sussman[23] (kHz)	Present Results (kHz)
1685	148	135	200
1804	425	420/74	546/89
1931	712	711/103	849/126
2029	1040	1038	1282
2058	1960	1180	1351
2119	n/a	1500	1744
2605	n/a	n/a	n/a

One of the benefits of having the ability to more densely populate the projectile velocity parameter space is that transition points from one regime of stability to the next become clearer and the general morphology of the space begins to focus. In addition, transition points may be more finely interrogated by the quasi-1D simulation in order to observe the changing behavior of the flow in order to arrive at mechanisms for transition. With a more densely populated parameter space, trends not observed in previous work also appear. For example, the space takes on

something akin to a terraced appearance where there are distinct regions of stability with rapid transitions in some locations from one dominant frequency to the next (e.g. around 2000 m/s and 2080 m/s).

The basic transition mechanism at work in the observed results is an out-of-phase behavior of pressure waves generated by the new reaction fronts. For projectile velocities below 1650 m/s, the reaction front is observed to be smooth. If new reaction fronts are being created, they are imperceptibly low in amplitude and strength at the studied grid resolution. At the beginning of the regular regime zone, there are moderate amplitude reaction front features. Increasing the projectile velocity has the effect of creating additional reaction zones along the same reaction peninsula. This is due to the pressure waves generated by new reaction zones being significantly out-of-phase with the reflected pressure waves from the projectile surface. As velocity increases, new reaction fronts are created by out-of-phase waves propagating faster than expansion waves can relax the shock front. This causes a secondary, low-frequency oscillation to appear mainly between 1730 m/s and 1960 m/s upon which the higher-frequency regular instability is superimposed. The secondary oscillation dies out around the detonation velocity of the mixture (1957 m/s), but this may be coincidental. As the projectile velocity increases past 1960 m/s, where the classic, in-phase regular regime is re-established, a "terraced" trend of oscillation frequency versus projectile velocity occurs. The cause of this trend is again due to narrow velocity ranges where out-of-phase pressure wave behavior creates new reaction fronts in addition to ones already being created periodically due to the classic regular regime mechanism. The reaction front at the transition points shows mixed regular regime behavior with non-cohesive, irregular reaction fronts created by the out-of-phase pressure waves. In general, as the projectile velocity increases, the amplitude of the reaction front is found to decrease, eventually smoothing out into apparently stable behavior as it begins to couple with the shock front.

Comparison of Present Results to 1D Mechanism Models

The simulated experiments of Ruegg and Dorsey are now reexamined in order to compare the present quasi-1D numerical results to published 1D instability mechanism models in the literature. First, the quasi-1D simulation of the regular, unsteady regime is compared with the published mechanism of Matsuo[26] in Figure 8. Note that all of the major features of the mechanism proposed by Matsuo are present in the simulated result. A newly created reaction front produces pressure waves that travel downstream toward the projectile surface and upstream toward the bow shock. The upstream traveling pressure wave meets the bow shock roughly in phase with the pressure wave reflected from the projectile surface. The collision of the pressure waves and the shock front causes the shock to move upstream with a contact discontinuity reflected downstream. The contact discontinuity is visible on the density plot and is visible as a line traced from each cusp of the bow shock to the newly created reaction front. The hot gas upstream of the contact discontinuity has a lower induction time than the downstream gas, which creates a new reaction zone that eventually extinguishes the old one. This process repeats indefinitely for a projectile with constant velocity. The simulated result differs slightly from the published mechanism in that the simulated contact discontinuity is connected to the tip of the reaction zone peninsula versus the 1D mechanism, which traces it to the point where the old reaction front is merged with the new one. In addition, the presently simulated result indicates that the reflected pressure waves skip a generation of new reaction zone before interacting with the bow shock. The published mechanism shows the reflected pressure wave interacting with the bow shock along with the upstream-traveling pressure wave of the next reaction zone generation. Finally, the present computations show a rarefaction wave reflected at the point where the pressure wave and the bow shock meet, which is not depicted in the published model.

The quasi-1D simulation of the large-disturbance, unsteady regime, shown with a density contour plot, will now be compared with the corresponding mechanism of Matsuo and Fujii[22] in Figure 9. The large-disturbance mechanism of Matsuo and Fujii requires an energy release large enough to create a deflagration to detonation transition (DDT), noted in the figure as an "explosion in an explosion" (this is discussed further in the detonation literature[27, 28]. This causes a penetration of the self-propelled reaction front through the bow shock, reflecting a rarefaction wave and contact discontinuity downstream at the point of intersection. The self-propelled reaction front, which is coupled with the bow shock for a short time, gradually separates from the shock wave and relaxes to its original position before resuming the cycle. Comparing the present results to the 1D mechanism shows that all of the essential features of the mechanism are reproduced in the quasi-1D simulation. Figure 10 shows a detailed view of the detonation region of the quasi-1D simulation to examine what is happening closer to the shock wave penetration. Here it is clearly visible that the intersection of the reaction shock wave from the first explosion with the bow shock is responsible for generating the rarefaction wave and the contact discontinuity that causes the second explosion. The second pressure wave seen in the simulated results is due to the generation of the second explosion, explaining why it doesn't appear in the general, single-explosion mechanism. After the second explosion, the pressure wave and reaction front traveling upstream merge with the bow shock and a self-sustained superdetonation

is observed for a short amount of time. Overall the quasi-1D simulation shows excellent agreement with the 1D mechanism found in the literature.

Further Parametric Assessment

While the quasi-1D formulation is capable of rapidly evaluating the effect of many parameters relevant to the stability of the reaction front, for brevity only one case study is shown here. A point of comparison with the previously presented Lehr results can be made by adjusting the freestream stoichiometry to be either lean or rich to study the effect on the behavior of the reaction front. For this comparison three cases were chosen across the velocity range studied by Lehr and the freestream stoichiometry was set to 0.80 for the lean case and 1.20 for the rich case. All other quantities (e.g. velocity, pressure, temperature) were held the same as in experiments. In general, for hydrogen-air, it was found that lean freestream conditions shifted the behavior of a particular projectile velocity case to a higher effective velocity while rich conditions shifted the behavior to a lower effective velocity. For example, for a projectile velocity of 1696 m/s, the stoichiometric freestream behavior is in a regular unsteady regime. Shifting the freestream stoichiometry to a value of 0.80 results in two frequency behavior while shifting the stoichiometry to 1.2 causes the reaction front to be completely stable. This behavior is due to the fact that the molecular weight of a lean fuel-air mixture increases for a lighter-than-air fuel such as hydrogen and the gas constant of the mixture increases accordingly. Because temperature, pressure, and velocity are being held constant, the freestream Mach number of the flow drops with increasing gas constant. This decrease in Mach number causes lower post-shock temperatures which increases the induction time, shifting the behavior of the reaction front to an effective lower velocity compared to the baseline stoichiometric results. By the same logic a mixture that is fuel lean for a lighter-than-air fuel would have an effective higher velocity compared to the stoichiometric baseline. Note that the trends stated here would presumably be the opposite for a heavier than air fuel.

V. Summary and Conclusions

A quasi-1D formulation has been developed that provides equations describing axisymmetric flow valid in the stagnation region of a sphere. The equations used in this formulation were derived by applying a local similarity postulate to the axisymmetric Navier Stokes equations. In order to evaluate the validity of this formulation, a number of cases of spherical projectiles fired into hydrogen/air mixtures at hypersonic velocities were simulated inviscidly to compare against existing experimental and numerical studies. The first comparison showed a qualitative agreement between the quasi-1D simulation and selected experiments by Ruegg and Dorsey[4] that showed stable; regular, unsteady; and large-disturbance, unsteady behavior. In addition, large-disturbance results were compared to the numerical work of Matsuo and Fujii[22] which showed a qualitative agreement of the time evolution of the reaction and shock fronts. The second comparison took place over a range of projectile velocities encompassing the experiments conducted by Lehr[6]. Numerical results by Sussman[23] were also included as an additional point of comparison. The velocity range was simulated densely by the quasi-1D code and at each point the frequency of the reaction front was recorded and compared to the experimental and higher-fidelity results. The general behavior of the reaction and shock fronts was captured over the velocity range in the present simulations and a reasonable agreement was obtained with recorded frequencies. The current simulations also showed trends not visible from the previous experimental and numerical results, warranting further investigation. Next, the simulated behaviors of the regular and large-disturbance instability regimes were compared against 1D mechanism models present in the literature. It was found that all of the important flow features in the published models were captured by the quasi-1D formulation. Finally, the effect of equivalence ratio on flow behavior was evaluated. It was found that the reaction front was quite sensitive to inflow stoichiometry due to its effect on induction time.

The present results are promising in establishing the quasi-1D formulation in rapidly evaluating premixed, shock-induced combustion flows, an important step toward understanding the behaviors of such flows over a large design space relevant to the operation of hypervelocity engines using PMSIC. Identifying regimes of predictably safe, steady behavior for conditions typically found at the entrance of the combustor is important in order to ensure feasible engine designs. In addition, understanding the mechanisms that cause large amplitude instabilities are helpful in avoiding or attempting to mitigate such behaviors. Overall, results from the quasi-1D analysis show promise as a valid starting point for analysts and designers in effectively conducting high-fidelity analyses and in the design of next-generation hypervelocity, airbreathing engines.

References

[1] Menees, G. P., Adelman, H. G., Bowles, J. V., and Cambier, J.-L., Wave combustors for trans-atmospheric vehicles, *Journal of Propulsion and Power*, Vol. 8, No. 3, May 1992, pp. 709–713.

[2] Rubins, P. M. and Bauer, R. C., A hypersonic ramjet analysis with premixed fuel combustion, *AIAA 2nd Propulsion Joint Specialist Conference*, AIAA 66-648, June 1966.
[3] Kumar, A. and Singh, D. J., Unsteady shock-induced combustion past blunt bodies, *Transition, Turbulence, and Combustion, Vol. II*, edited by M. Y. Hussaini, T. B. Gatski, and T. L. Jacobson, Kluwer Academic Publishers, 1994, pp. 289–296.
[4] Ruegg, F. W. and Dorsey, W. W., A missile technique for the study of detonation waves, *Journal of research of the National Bureau of Standards*, Vol. 66C, 1961, pp. 51–58.
[5] McVey, J. B. and Toong, T. Y., Mechanism of instabilities of exothermic hypersonic blunt-body flows, *Combustion Science and Technology*, Vol. 3, 1971, pp. 63–76.
[6] Lehr, H. F., Experiments on Shock-Induced Combustion, *Astronautica Acta*, Vol. 17, 1972, pp. 589–597.
[7] Alpert, L. R. and Toong, T. Y., Periodicity in exothermic hypersonic flows about blunt projectiles, *Acta Astronautica*, Vol. 17, Sept. 1972, pp. 539–560.
[8] Matsuo, A. and Fujiwara, T., Numerical simulation of shock-induced combustion around an axisymmetric blunt body, *AIAA 26th Thermophysics Conference*, AIAA-91-1414, June 1991.
[9] Matsuo, A., Fujii, K., and Fujiwara, T., Computational study of unsteady combustion around projectiles with emphasis on the large-disturbance oscillation, *32nd Aerospace Sciences Meeting & Exhibit*, AIAA-94-0764, Jan. 1994.
[10] Wilson, G. J. and Maccormack, R. W., Modeling supersonic combustion using a fully implicit numerical method, *AIAA Journal*, Vol. 30, No. 4, April 1992, pp. 1008–1015.
[11] Jachimowski, C. J., An Analytical Study of the Hydrogen-Air Reaction Mechanism With Application to Scramjet Combustion, Tech. Rep. TP-2791, NASA Langley Research Center, 1988.
[12] Wilson, G. J. and Sussman, M. A., Computation of unsteady shock-induced combustion using logarithmic species conservation equations, *AIAA Journal*, Vol. 31, No. 2, Feb. 1993, pp. 294–301.
[13] Ahuja, J. K., Tiwari, S. N., and Singh, D. J., Hypersonic Shock-Induced Combustion in a Hydrogen-Air System, *AIAA Journal*, Vol. 33, No. 1, 1994, pp. 173–176.
[14] Ahuja, J. K. and Tiwari, S. N., Numerical simulation of shock-induced combustion in a superdetonative hydrogen-air system, *31st Aerospace Sciences Meeting & Exhibit*, AIAA-93-0242, AIAA, Jan. 1993.
[15] Ahuja, J. K. and Tiwari, S. N., Investigation of shock-induced combustion past blunt projectiles, Tech. Rep. CR-4724, NASA Langley Research Center, April 1996.
[16] Kao, H. C., Hypersonic viscous flow near the stagnation streamline of a blunt body: I. A test of local similarity, *AIAA Journal*, Vol. 2, No. 11, 1964, pp. 1892–1897.
[17] Kumar, A., *Hypersonic rarefied transition on blunt and slender bodies*, Ph.D. thesis, 1973.
[18] MacCormack, R. W., The effect of viscosity in hypervelocity impact cratering, *AIAA Hypervelocity Impact Conference*, AIAA-69-354, 1969.
[19] Singh, D. J., Carpenter, M. H., and Kumar, A., Numerical Simulation of Shock-Induced Combustion/Detonation in a Premixed H2-Air Mixture Using Navier-Stokes Equations, *27th Joint Propulsion Conference*, AIAA-91-3359, AIAA/SAE/ASME, June 1991.
[20] Mott, D., A Quasi-Steady-State Solver for the Stiff Ordinary Differential Equations of Reaction Kinetics, *Journal of Computational Physics*, Vol. 164, No. 2, Nov. 2000, pp. 407–428.
[21] Gardiner, W. C., editor, *Combustion Chemistry*, Springer-Verlag, 1984.
[22] Matsuo, A. and Fujii, K., Detailed Mechanism of the Unsteady Combustion Around Hypersonic Projectiles, *AIAA Journal*, Vol. 34, No. 10, Oct. 1996, pp. 2082–2089.
[23] Sussman, M. A., A computational study of unsteady shock induced combustion of hydrogen-air mixtures, *30th Joint Propulsion Conference*, AIAA-94-3101, June 1994.
[24] Gordon, S. and McBride, B. J., Computer Program for Calculation of Complex Chemical Equilibrium Compositions and Applications I. Analysis, Tech. Rep. RP-1311, NASA, Oct. 1994.
[25] McBride, B. J. and Gordon, S., Computer Program for Calculation of Complex Chemical Equilibrium Compositions and Applications II. User's Manual and Program Description, Tech. Rep. RP-1311-P2, NASA, June 1996.
[26] Matsuo, A. and Fujii, K., Computational Study of Large-Disturbance Oscillations in Unsteady Supersonic Combustion Around Projectiles, *AIAA Journal*, Vol. 33, No. 10, Oct. 1995, pp. 1828–1835.
[27] Oppenheim, A. K., Manson, N., and Wagner, H. G., Recent Progress in Detonation Research, *AIAA Journal*, 1963, pp. 2243–2252.
[28] Urtiew, P. A. and Oppenheim, A. K., Experimental observations of the transition to detonation in an explosive gas, *Proceedings of the Royal Society of London*, Vol. 295, Nov. 1966.

Figures

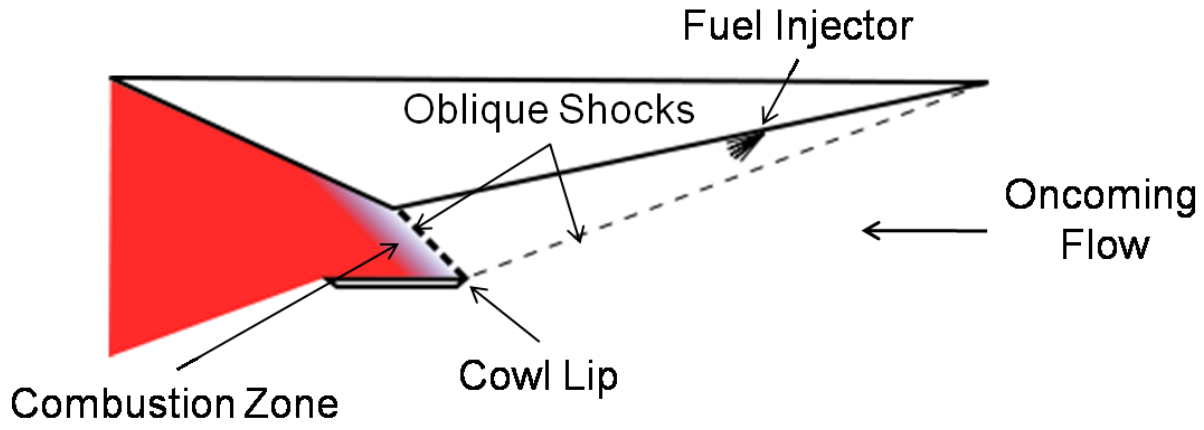

Figure 1. A schematic is shown for a hypervelocity vehicle using premixed, shock-induced combustion.

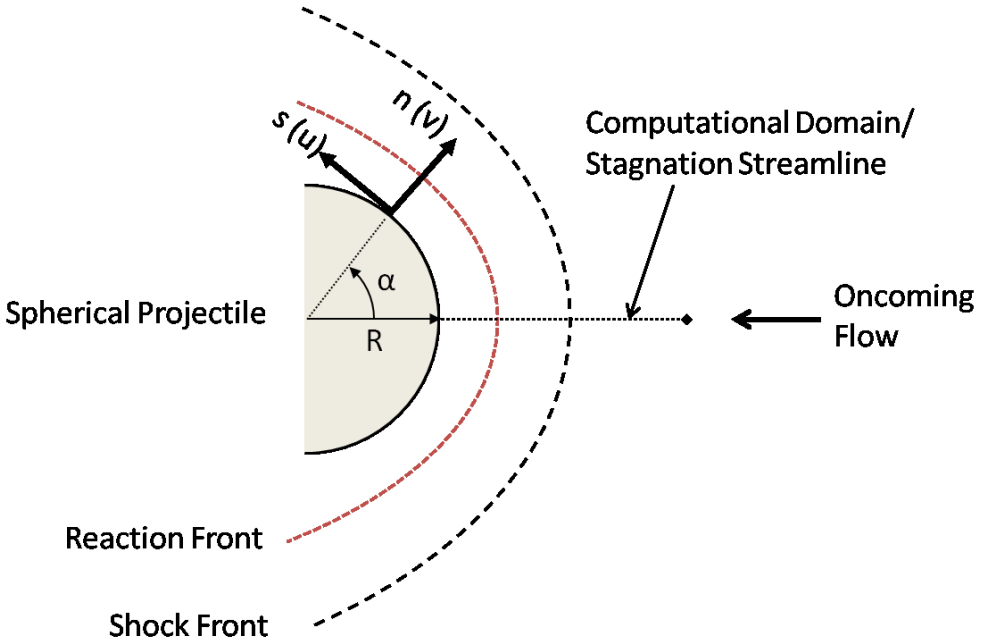

Figure 2. The problem setup for this study is shown.

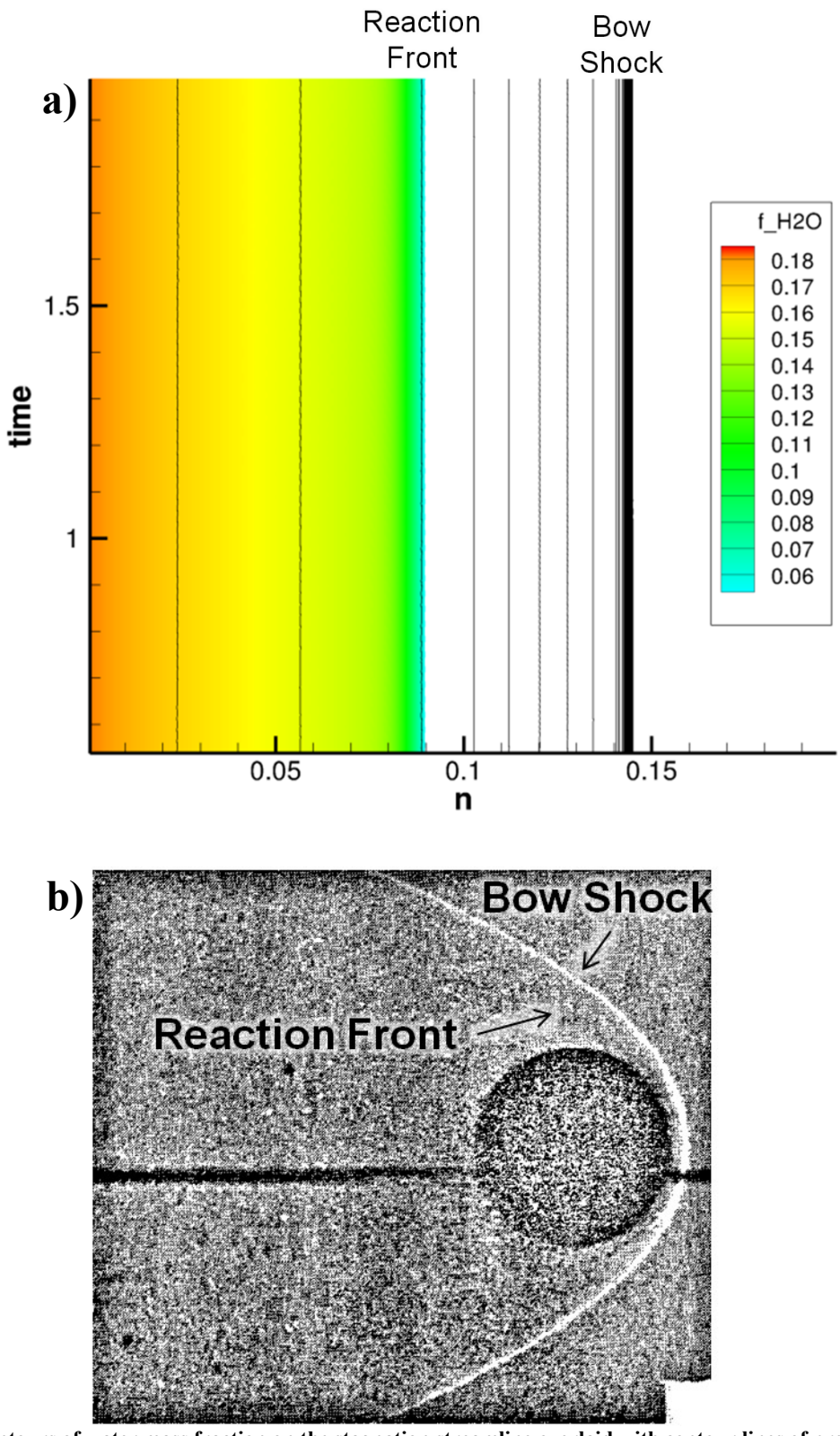

Figure 3. a) Contours of water mass fraction on the stagnation streamline overlaid with contour lines of pressure as a function of non-dimensional time for Ruegg and Dorsey experiment Case 1. b) An annotated experimental shadowgraph captured by Ruegg and Dorsey for the same conditions is shown for comparison[4].

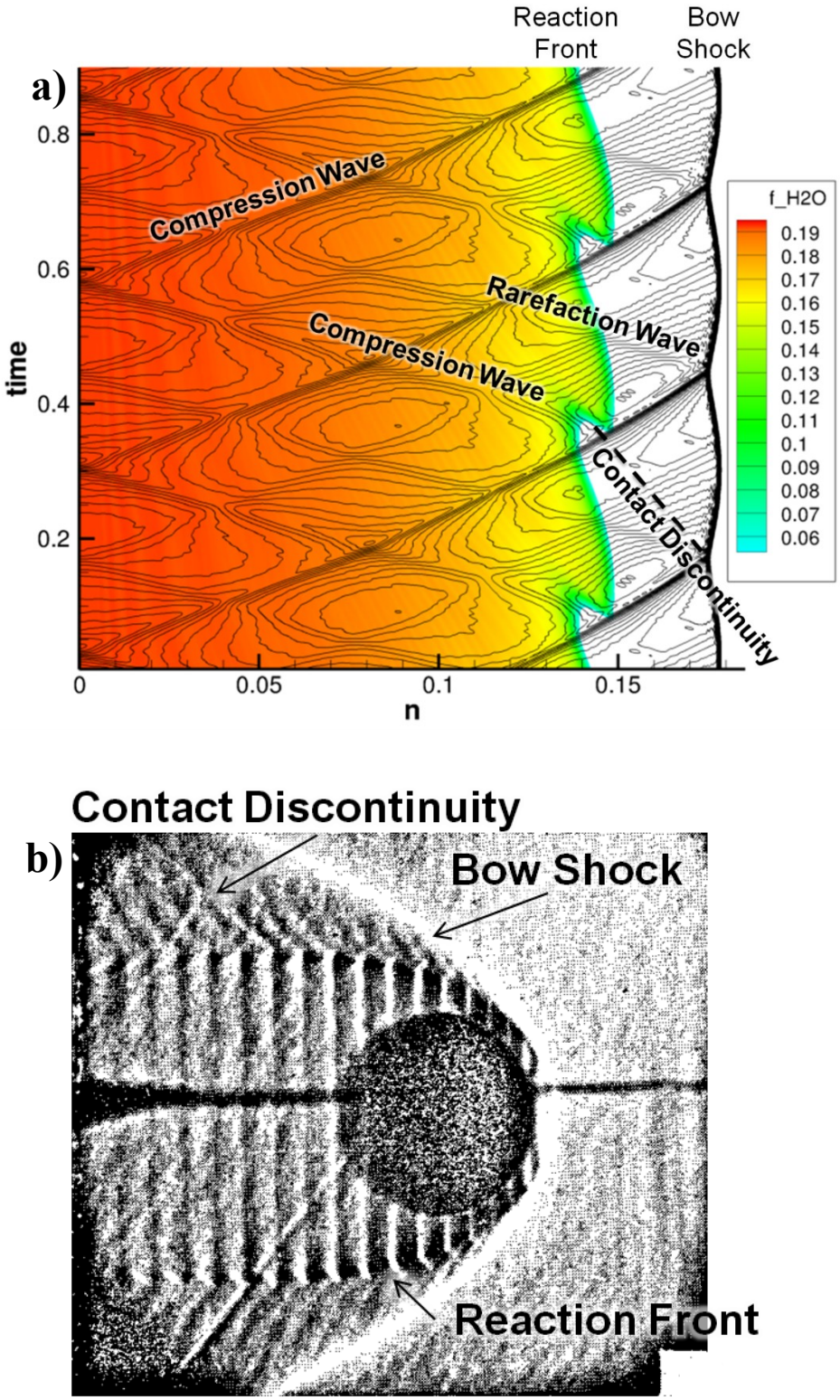

Figure 4. a) Contours of water mass fraction on the stagnation streamline overlaid with contour lines of pressure as a function of non-dimensional time for Ruegg and Dorsey experiment Case 2. The drawn contact discontinuity is approximated based on separate density contours. b) An annotated experimental shadowgraph captured by Ruegg and Dorsey for the same conditions is shown for comparison[4].

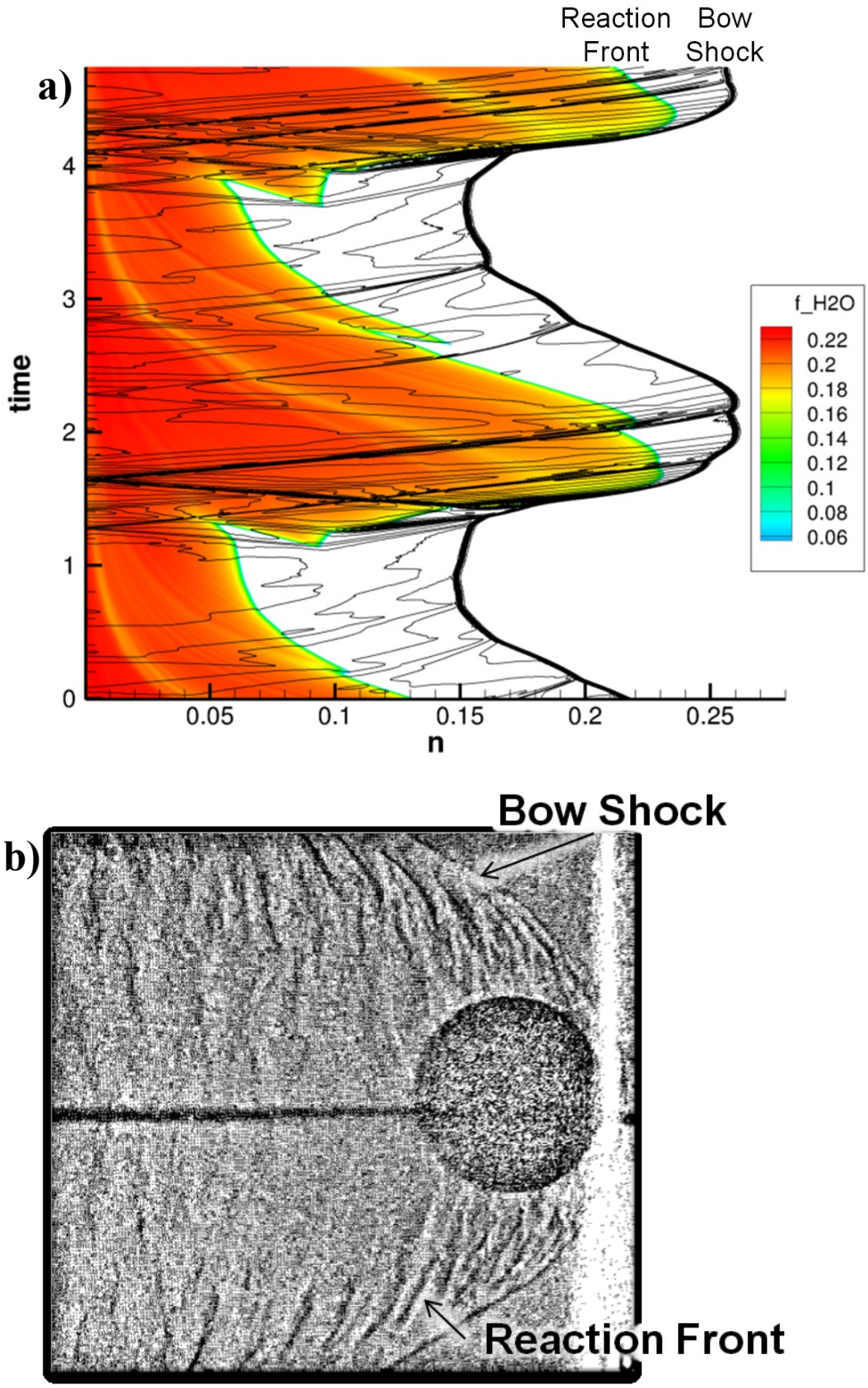

Figure 5. a) Contours of water mass fraction on the stagnation streamline overlaid with contour lines of pressure as a function of non-dimensional time for Ruegg and Dorsey experiment Case 3. b) An annotated experimental shadowgraph captured by Ruegg and Dorsey for the same conditions is shown for comparison[4].

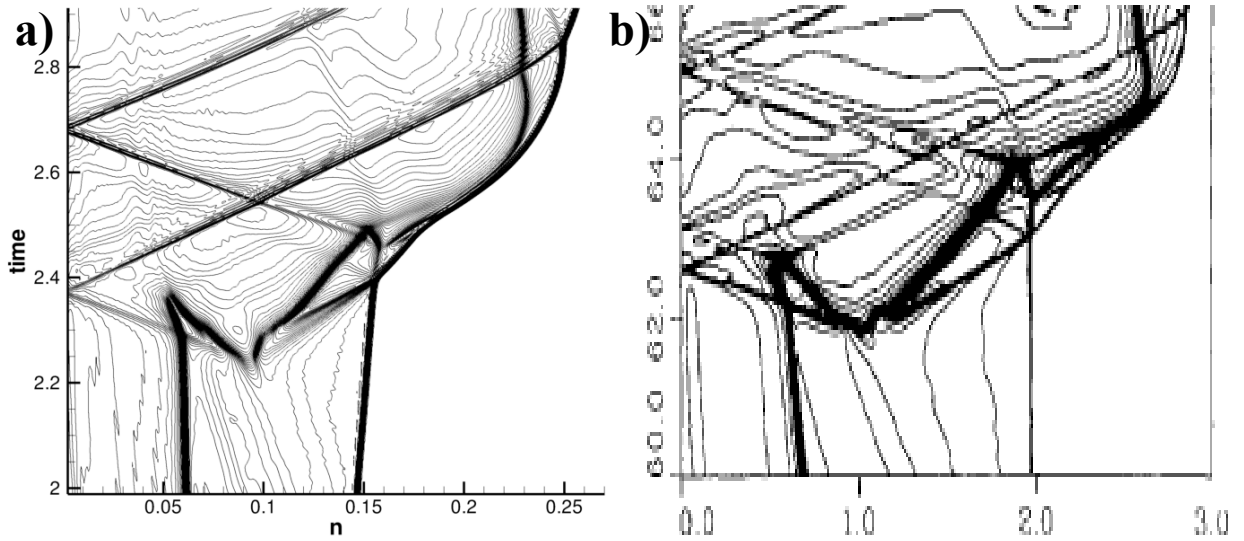

Figure 6. A detail view of density contours on the stagnation streamline as a function of time for Case 3 for the a) present quasi-1D simulation and b) high-fidelity, 2D simulation conducted by Matsuo and Fujii[22] (reproduced with permission). Note that the computed results are non-dimensional in time while the high-fidelity plot is in seconds.

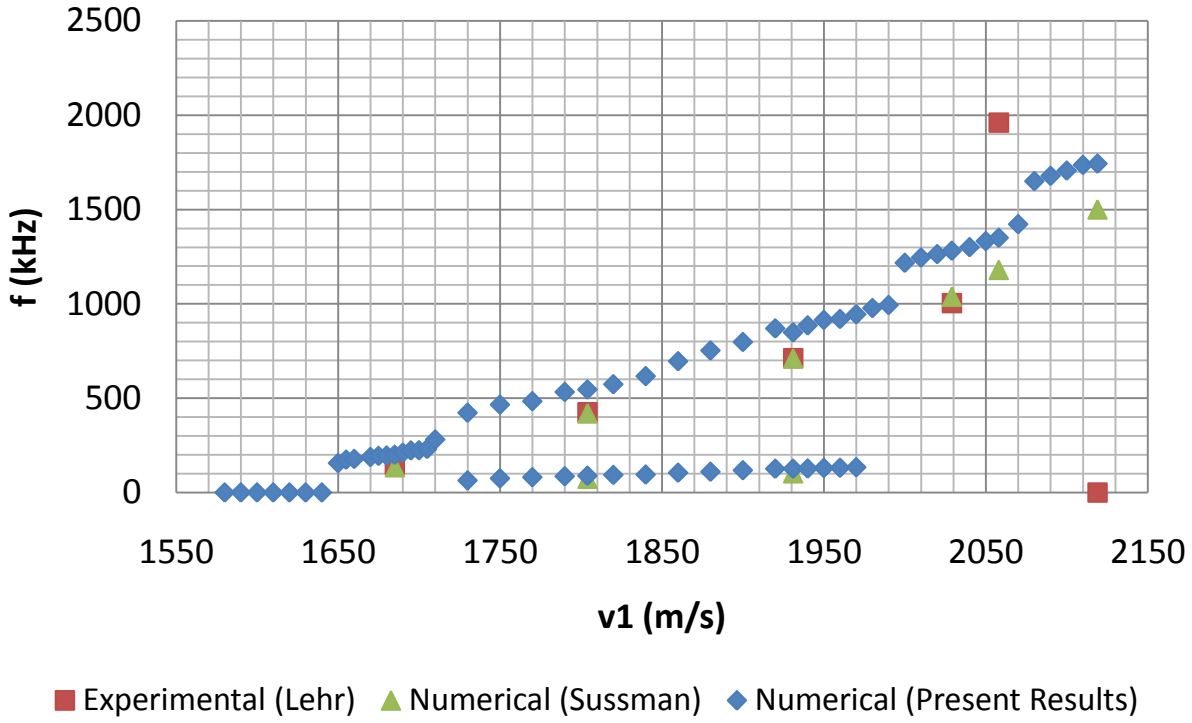

Figure 7. Reaction front oscillation frequency as a function of projectile velocity for experimental and numerical investigations.

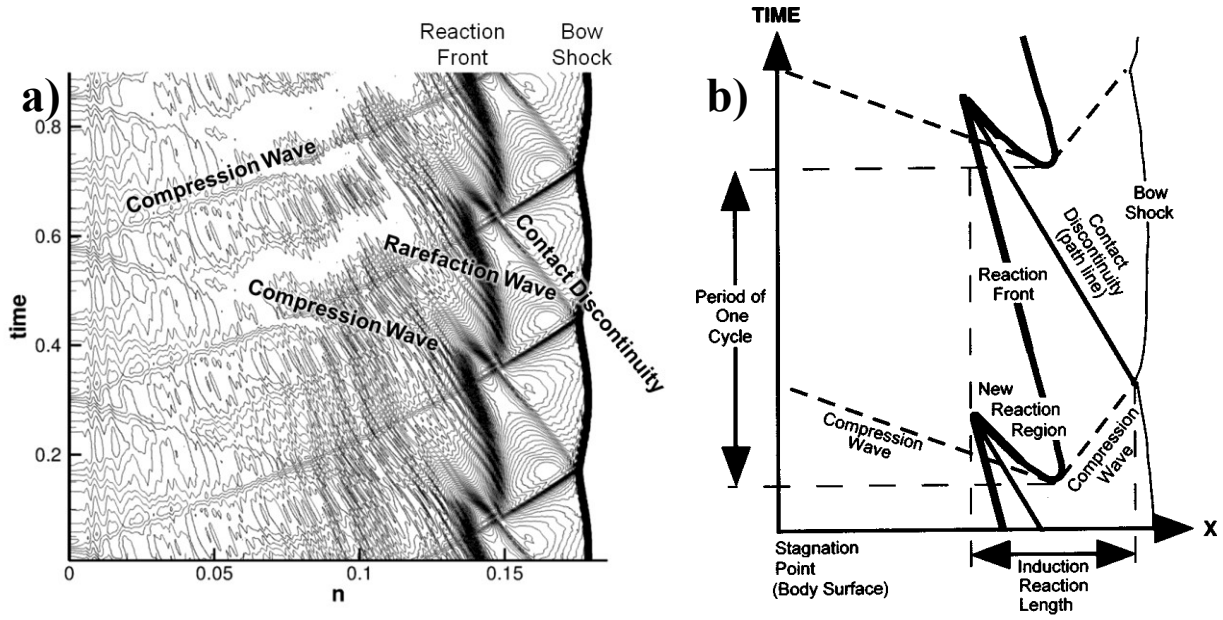

Figure 8. Contour lines of a) density on the stagnation streamline as a function of time for Ruegg and Dorsey experiment Case 2 and b) 1D mechanism for the regular, unsteady regime by Matsuo[8] (reproduced with permission).

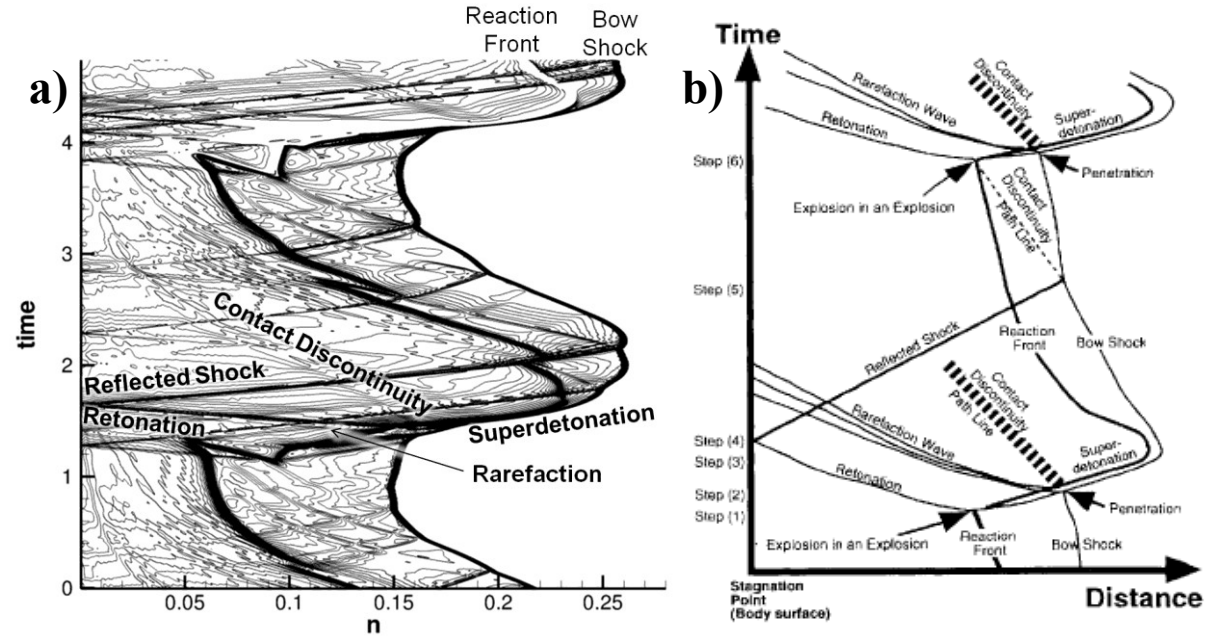

Figure 9. Contour lines of a) density on the stagnation streamline as a function of time for Ruegg and Dorsey experiment Case 2 and b) 1D mechanism for the large-disturbance, unsteady regime by Matsuo and Fujii[22] (reproduced with permission).

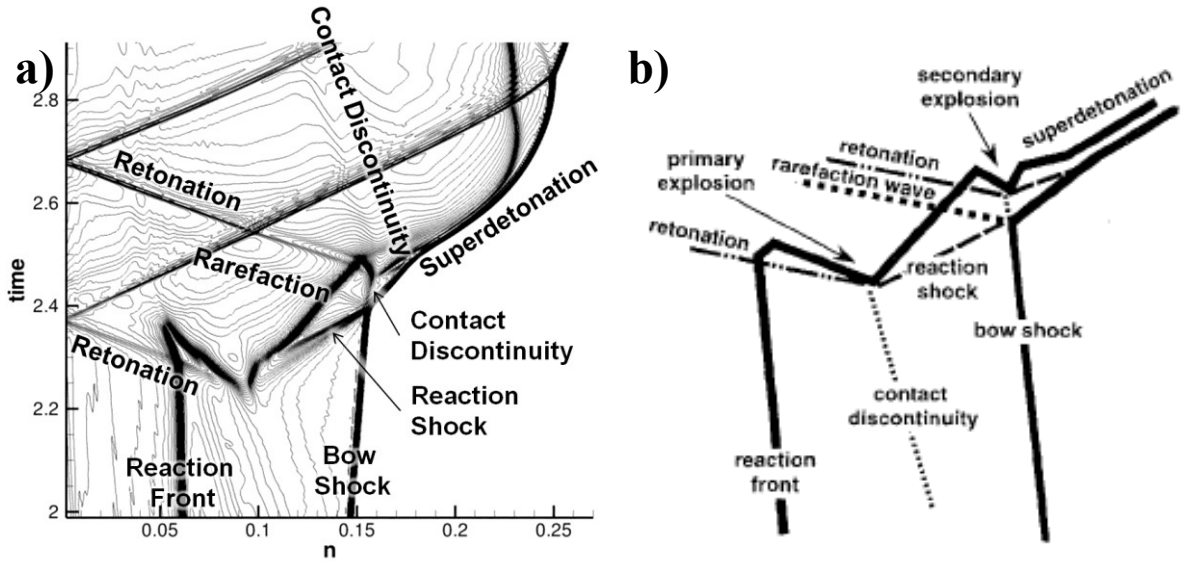

Figure 10. A detail view of the a) stagnation streamline density contours from the present simulation (Case 3) compared to a b) 1D sub-mechanism of the large-disturbance regime as proposed by Matsuo and Fujii[22] (reproduced with permission).